Electronic Supplementary Information

The unexpected mechanism of transformation from conventional room-temperature phosphorescence to TADF-type organic afterglow triggered by simple chemical modification

Minjian Wu,[a,b] Jiuyang Li,[a] Ju Huang,[a] Xuepu Wang,[a] Guangming Wang,[a] Xiuzheng Chen,[a] Xun Li,[a] Xuefeng Chen,[a] Shuhui Ding,[a] Hefeng Zhang*[b] and Kaka Zhang*[a]

a. Key Laboratory of Synthetic and Self-Assembly Chemistry for Organic Functional Molecules, Shanghai Institute of Organic Chemistry, University of Chinese Academy of Sciences, Chinese Academy of Sciences, 345 Lingling Road, Shanghai, 200032, People's Republic of China. E-mail: zhangkaka@sioc.ac.cn

b. Department of Chemistry and Key Laboratory for Preparation and Application of Ordered Structural Materials of Guangdong Province, College of Science, Shantou University, Shantou 515063, People's Republic of China. Email: hfzhang@stu.edu.cn

Experimental Section

Materials

Coronene (95%+, alpha chemical), acetic anhydride (98.5%, Sinopharm Chemical Reagent), boron trifluoride diethyl etherate (98%, TCI), benzophenone (BP) (99%, Macklin), and 4-methoxybenzophenone (MeOBP) (99%, Innochem), phenyl benzoate (PhB) (99%, Energy Chemical), 4-bromobenzophenone (BrBP) (98%, Innochem), Pluronic F127 (Sigma), rhodamine 6G, (97%, Aladdin), benzoic acid (99.5%+, Sinopharm Chemical Reagent), salicylic acid (99.7%, Dibo Chem), syringic acid (98%+, Dibo Chem), 1,4-dimethoxybenzene (99%, Adamas), 4-methylbenzophenone (MeBP) (98%, Innochem), 4-benzoylbiphenyl (98%, Ark), 4-bromodibenzofuran (98%, Leyan reagent), dibenzothiophene (98%, Aladdin).

Physical measurements and instrumentation

^{1}H NMR (400 MHz), and ^{19}F NMR (376 MHz) spectra were recorded on a JEOL Fourier-transform NMR spectrometer (400 MHz). Mass spectra were performed on Agilent Technologies 5973N and Thermo Fisher Scientific LTQ FT Ultras mass spectrometer. FT-IR spectra were recorded on a Nicolet AVATAR-360 FT-IR spectrophotomerter with a resolution of 4 cm^{-1}. UV-Vis absorption spectra were recorded on a Hitachi U-3310 UV-vis spectrophotometer and a Techcomp UV1050 UV-vis spectrophotometer. The steady-state and delayed emission spectra were collected by Hitachi FL-4700 fluorescence spectrometer equipped with chopping systems; the delayed emission spectra were obtained with a delay time of approximately 1 ms. The excited state decay profiles in millisecond to second region were collected by Hitachi FL-4700 fluorescence spectrometer equipped with chopping systems. The fluorescence decay profiles in nanosecond region were recorded by using time-correlated single photon counting technique (TCSPC) on a Edinburgh FLS1000 fluorescence spectrometer equipped with a picosecond pulsed diode laser. Photoluminescence quantum yield was measured by a Hamamatsu absolute PL quantum yield measurement system based on a standard protocol. Photographs and videos were captured by iphone 12 and Redmi K20 pro cameras. Before imaging, samples were irradiated by a 365 nm UV lamp (5 W) for approximately 5 s at a distance of approximately 15 cm. All animal procedures were reviewed and approved by the Institutional Animal Care and Use Committee at Chinese Academy of Sciences and are in accordance with the Guide for the Care and Use of Laboratory Animals of Chinese Academy of Sciences.

TD-DFT calculations

TD-DFT calculations were performed to study the photophysical properties of molecularly dispersed Cor, $CorBF_2$, and R_1 in the solid state. Since the afterglow

properties are originated from the excited states of molecularly dispersed Cor, $CorBF_2$ and R_1 in the rigid MeOBP matrices where intramolecular rotation and vibration are largely restricted, the optimized geometry of Cor, $CorBF_2$ and R_1 ground state were used for all the TD-DFT calculations. The optimized geometry of Cor, $CorBF_2$ and R_1 ground state were obtained by a DFT calculation on Gaussian 16 program (Revision A.03) using B3LYP functional and 6-31G(d,p) basis set. The singlet excited states and triplet excited states were calculated on ORCA 4.2.1 program with B3LYP/G functional and def2-TZVP(-f) basis set. Spin-orbit coupling (SOC) matrix elements between the singlet excited states and triplet excited states were calculated with spin-orbit mean-field (SOMF) methods on ORCA 4.2.1 program with B3LYP/G functional and def2-TZVP(-f) basis set. The obtained electronic structures were analyzed by Multiwfn software. All isosurface maps to show the electron distribution and electronic transitions were rendered by Visual Molecular Dynamics (VMD) software based on the exported files from Multiwfn. (F. Neese, *Wiley Interdiscip. Rev.: Comput. Mol. Sci.* **2018**, *8*, 1327-1332; A. D. Becke, *Phys. Rev. A* **1988**, *38*, 3098-3100; C. Lee, W. Yang, R. G. Parr, *Phys. Rev. B* **1988**, *37*, 785-789; B. Miehlich, A. Savin, H. Stoll, H. Preuss, *Chem. Phys. Lett.* **1989**, *157*, 200-206; F. Weigend, R. Ahlrichs, *Phys. Chem. Chem. Phys.* **2005**, *7*, 3297-3305; T. Lu, F. Chen, *J. Comput. Chem.* **2012**, *33*, 580-592; W. Humphrey, A. Dalke, K. Schulten, *J. Mol. Graphics* **1996**, *14*, 33-38).

Synthesis of $CorBF_2$ via cascade reaction

Into a round bottom flask were added coronene (300 mg, 1.0 mmol), acetic anhydride (4 mL) and boron trifluoride diethyl etherate (0.7 mL). The reaction mixture was heated to 82 ℃ and stirred for 4-5 h. Then the reaction was quenched by adding the reaction mixture dropwise into cold water. The precipitates were washed by water for three times and dried under vacuum. The crude product was purified by column chromatography over silica gel using petroleum ether/dichloromethane (2:1-1:2) as eluent to give orange solids with an isolation yield of ~10%. The $CorBF_2$

was further purified by three cycles of recrystallization in spectroscopic grade dichloromethane/hexane. ^{1}H NMR (400 MHz, DMSO-d6) δ 9.53 (s, 1H), 9.37 (d, J = 9.0 Hz, 1H), 9.12-8.95 (m, 9H), 7.52 (s, 1H), 2.72 (s, 3H). ^{19}F NMR (376 MHz, DMSO-d6), δ -135.23 (20%), -135.29 (80%), relative to $CFCl_3$ /ppm. ^{13}C NMR Spectra were very weak because of the poor solubility of $CorBF_2$. FT-IR (KBr, cm^{-1}): ν 3020, 1908, 1609, 1457, 1433, 1391, 1338, 1304, 1162, 1066, 1046, 1026, 980, 910, 848, 816, 760, 688, 605, 578, 547, 489, 473. LRMS, m/z 432. HRMS (negative ESI) m/z found (calcd for $C_{28}H_{14}O_2{}^{10}BF_2$) 430.1097 (430.1098).

Synthesis of R_1 via aldol condensation

For the synthesis of R_1, into a round bottom flask were added $CorBF_2$ (0.185 mmol, 80 mg), *p*-dimethylaminobenzaldehyde (0.536 mmol, 80 mg), *n*-butylamine (3.5 μL) and chloroform (5 mL). The reaction was refluxed at 65-70°C for 3-4 h. After cooling to room temperature, the solvent was removed by distillation under reduced pressure. Then the crude product was washed by toluene for three times with a yield of 71.38%, then the product was further purified by column chromatography using petroleum ether/dichloromethane (1:1) as eluent to give brownish green solids. After careful column chromatography, R_1 was further purified by recrystallization in dichloromethane/n-hexane. ^{1}H NMR (400 MHz, 1,1,2,2-tetrachloroethane-d2) δ 9.57 (d, *J* = 9.5 Hz, 1H), 9.32 (s, 1H), 9.14-8.86 (m, 9H), 8.30-8.22 (m, 1H), 7.64 (d, *J* = 9.2 Hz, 2H), 6.93-6.88 (m, 1H), 6.78-6.68 (m, 3H), 3.11 (s, 6H). ^{19}F NMR (376 MHz, 1,1,2,2-tetrachloroethane-d2), δ -139.21(20%), -139.27 (80%), relative to $CFCl_3$ /ppm. ^{19}F NMR spectrum of R_1 has been obtained by data accumulation for 1 hour (Figure S43). Since R_1 has low solubility in common organic solvents, we didn't obtain satisfactory ^{13}C NMR and ^{11}B NMR spectra of R_1. The ^{1}H NMR and ^{19}F NMR spectra, high-resolution MS studies and the reported studies (*Nat. Photonics.*, 2018, **12**, 98; *Angew. Chem. Int. Ed.*, 2021, **60**, 18630) support the success of the Aldol reaction between $CorBF_2$ and 4-dimethylaminobenzaldehyde to form R_1. The aromatic region of the ^{1}H NMR spectrum is clean without any signals from possible luminescence

impurity (Figure S42). In the main text, we also rule out the impurity mechanism for the afterglow in R_1-MeOBP system by careful analyses and discussion. FT-IR (KBr, cm^{-1}): ν 2908, 1597, 1521, 1489, 1474, 1436, 1397, 1369, 1339, 1326, 1290, 1276, 1197, 1166, 1153, 1135, 1052, 994, 946, 922, 857, 817, 753, 732, 691, 589, 553, 512, 419. LRMS, m/z 563. HRMS (positive ESI) m/z found (calcd for $C_{37}H_{24}O_2{}^{10}BF_2Na^+$): 585.1793 (585.1797).

Preparation of afterglow materials by doping BF_2bdk into organic matrices

For the preparation of CorBF_2-MeOBP-0.01% powders, 50 μL CorBF_2 in dichloromethane (0.2 mg/mL) and 1 mL MeOBP solution in dichloromethane (100 mg/mL) were added into an agate mortar (diameter = 5 cm). After grinding and solvent evaporating, CorBF_2-MeOBP-0.01% powders that show afterglow properties were obtained. The other afterglow materials in this paper with different doping concentrations, different BF_2bdk compounds and different organic matrices were prepared through similar processes.

Text S1. Advantages of TADF-type afterglow materials.

TADF-type organic afterglow materials have emerged as an important class of luminescent materials because of their potential to achieve highly efficient afterglow systems. Besides, compared to conventional RTP systems, the Stokes shift of the afterglow emission in TADF-type systems are much smaller. This would be useful for the fabrication of visible-light-excitable or long-wavelength-excitable afterglow materials, especially in the case of deep-blue RTP materials where high-energy UV excitation sources with short wavelengths such as 300 nm and even shorter are considered to be necessary in the reported studies. Moreover, if the TADF afterglow was used as donors for excited state energy transfer to fluorescence acceptors, the

spin-allowed singlet-to-singlet would give rise to high efficiency of excited state energy transfer to produce efficient long-wavelength afterglow materials. Furthermore, because of the smaller Stokes shift in TADF afterglow systems, the fabrication of blue and even purple afterglow materials would be not so difficult when compared to that in conventional RTP systems. Finally, the additional pathway to harvest triplet energies would also allow the fabrication of efficient long-wavelength afterglow materials (such as red afterglow materials and even NIR afterglow materials) to counteract with the energy gap law.

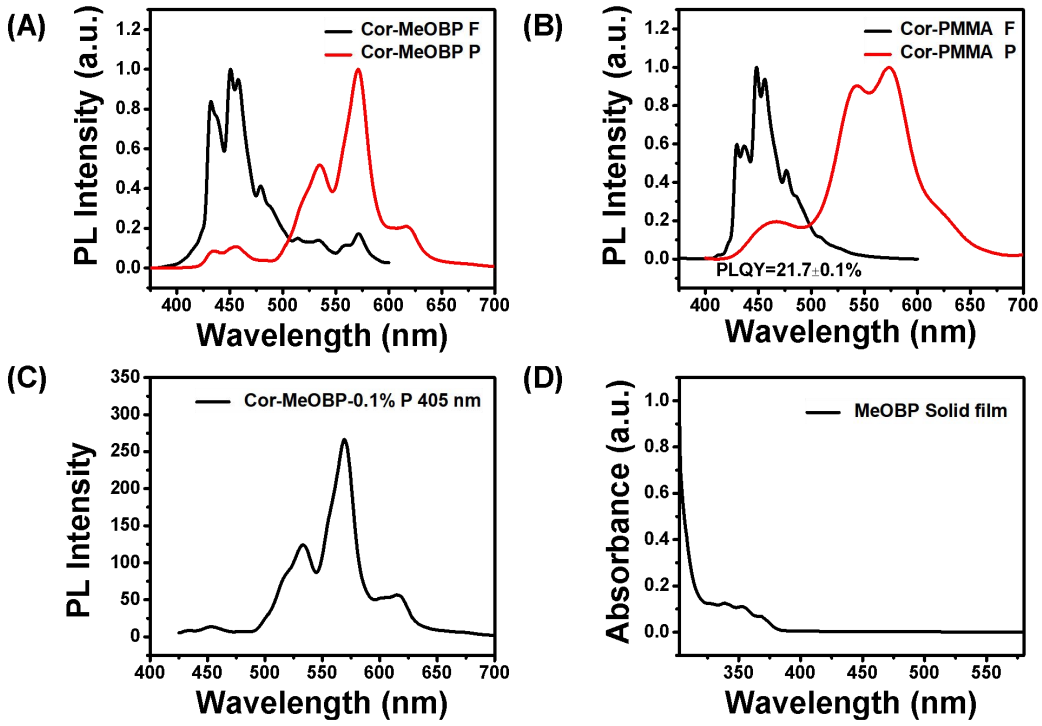

Figure S1: (A) Room-temperature steady-state and delayed emission spectra of the Cor-MeOBP materials. (B) Room-temperature steady-state and delayed emission spectra of the Cor-PMMA materials. (C) The delayed emission spectra (excited at 405 nm) of the Cor-MeOBP-0.1% materials. (D) The UV-vis spectra of the MeOBP solid film. Cor-PMMA materials have also been prepared and show similar fluorescence maxima to Cor-MeOBP materials (Figure S1A-B). These suggest the absence of intermolecular charge transfer between Cor and MeOBP. The Cor-MeOBP materials can be excited by 405 nm light to exhibit significant room-temperature phosphorescence (Figure S1C). Since MeOBP has negligible absorption at 405 nm (Figure S1D), these results suggest that the excited state energy transfer from MeOBP

to Cor may exist when the samples are excited at 365 nm but is not necessary for the emergence of organic room-temperature phosphorescence.

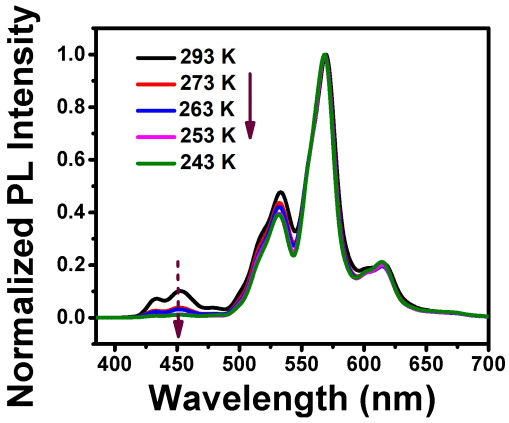

Figure S2. Variable temperature delayed emission (1 ms delay) spectra of Cor-MeOBP-0.1% materials.

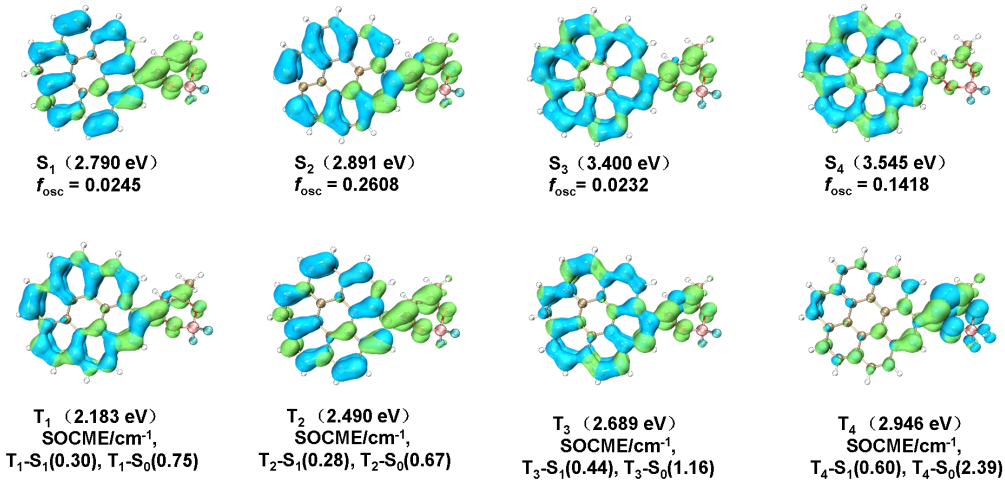

Figure S3. TD-DFT-calculated electron density difference of singlet and triplet excited states of $CorBF_2$.

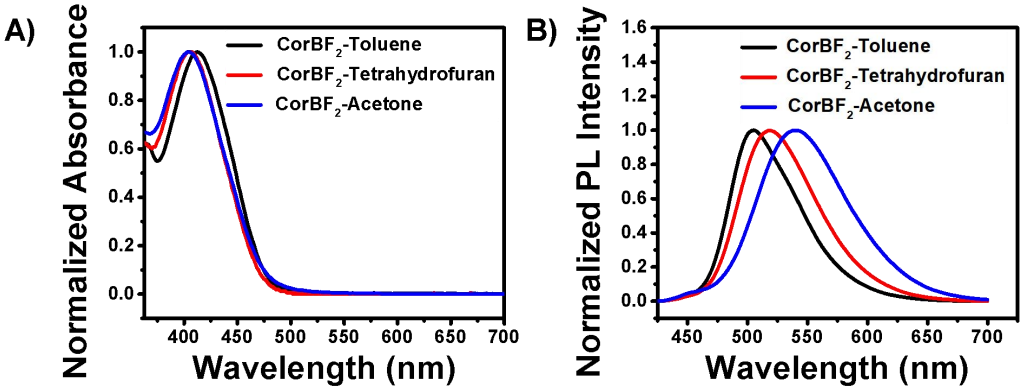

Figure S4. A) UV-Vis spectra of $CorBF_2$ in toluene, tetrahydrofuran and acetone solutions. B) Steady-state emission spectra of $CorBF_2$ in toluene, tetrahydrofuran and acetone solutions.

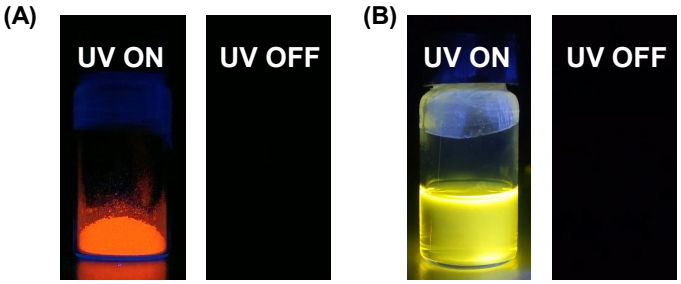

Figure S5. Photographs of $CorBF_2$ powders (A) and $CorBF_2$ in dichloromethane (B) at room temperature under 365 nm UV light and after removal of the UV light.

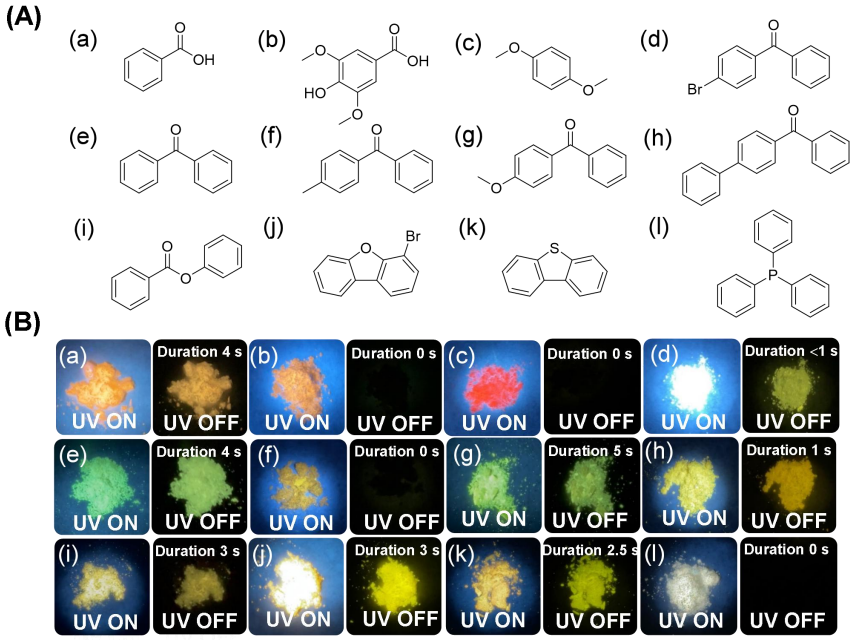

Figure S6. The chemical structural formula (A) of organic matrices and photographs (B) of $CorBF_2$-matrix-0.01% powders under 365 nm UV light and after removal of

the UV light. Duration refers to the lasting time of afterglow after removal of the UV light. The red, orange and yellow fluorescence and afterglow observed in some $CorBF_2$-Matrix-0.01% powders (red shifted when compared to $CorBF_2$-MeOBP-0.01% Powders) should be caused by molecular aggregation of $CorBF_2$ in matrices. In some organic matrices such as benzoic acid and others, it was found that $CorBF_2$ molecules with large π surface can still form aggregates at 0.01% doping concentration.

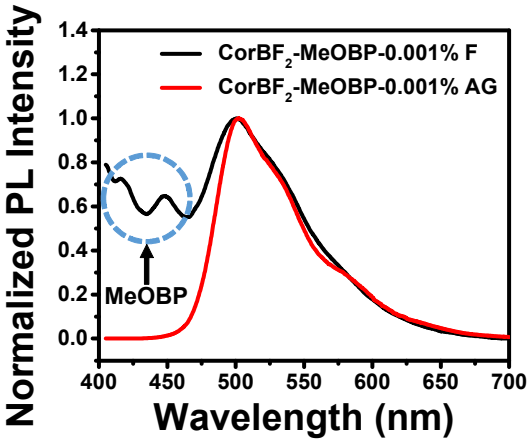

Figure S7. Room-temperature steady-state emission (black line) and delayed emission spectra (red line) of $CorBF_2$-MeOBP-0.001% powders.

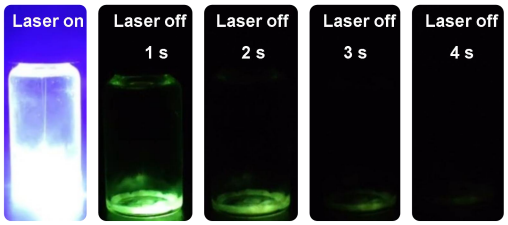

Figure S8. Photographs of $CorBF_2$-MeOBP-0.01% materials under 405 nm laser and after removal of excitation source.

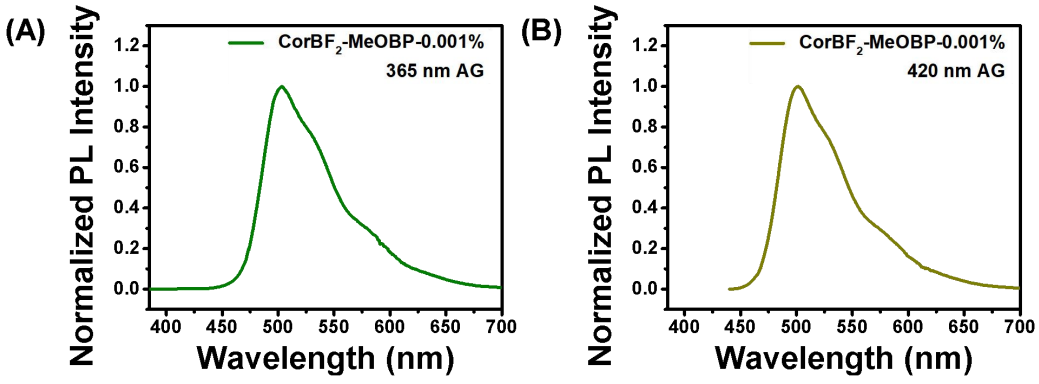

Figure S9. (A-B) Room-temperature delayed emission spectra of

$CorBF_2$-MeOBP-0.001% powders excited by 365 nm UV excitation source (A) and 420 nm visible light excitation source (B).

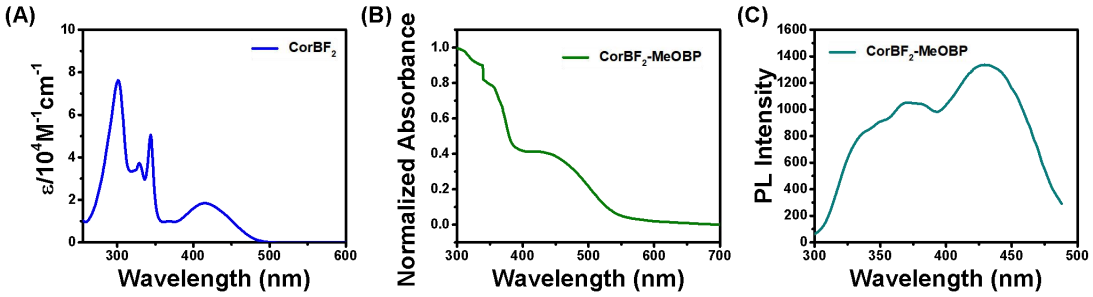

Figure S10. (A-C) UV-vis spectra of $CorBF_2$ in dichloromethane solutions (A), UV-vis spectra of $CorBF_2$-MeOBP melt-cast films (B) and excitation spectra (C) of $CorBF_2$-MeOBP samples.

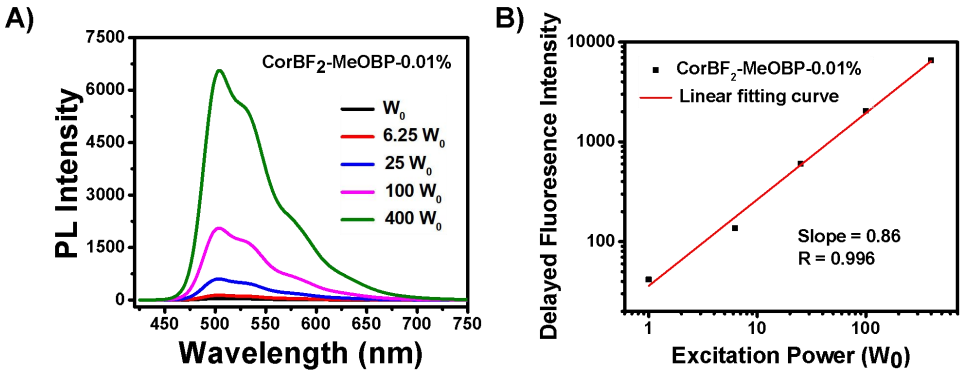

Figure S11. (A-B) Power-dependent delayed fluorescence spectra of $CorBF_2$-MeOBP-0.01% samples (A). It is found that delayed fluorescence intensity of the afterglow materials exhibit a quasi-linear dependence on the excitation dose, which further support the TADF mechanism (B).

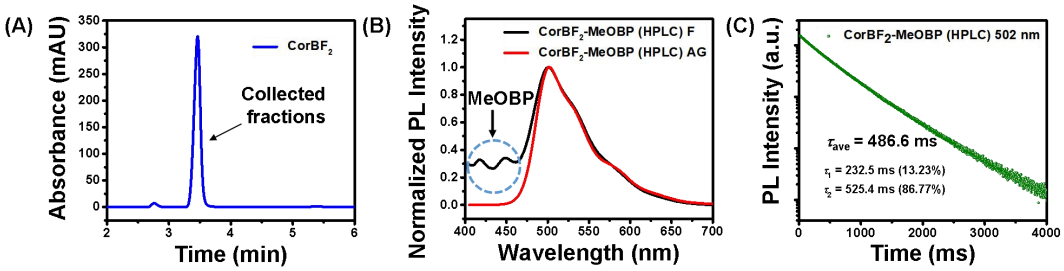

Figure S12. (A) The HPLC result of $CorBF_2$. (B) Room-temperature steady-state emission (black line) and delayed emission (red line) spectra of $CorBF_2$-MeOBP (HPLC) powders. (C) Room-temperature emission decay of $CorBF_2$-MeOBP (HPLC) materials monitored at 502 nm. The HPLC result showed a relatively high purity of $CorBF_2$. The $CorBF_2$-MeOBP (HPLC) materials were prepared by doping higher purity of $CorBF_2$ (separated and collected fractions through HPLC) into MeOBP

matrix, which exhibited excellent afterglow property similar to $CorBF_2$-MeOBP materials.

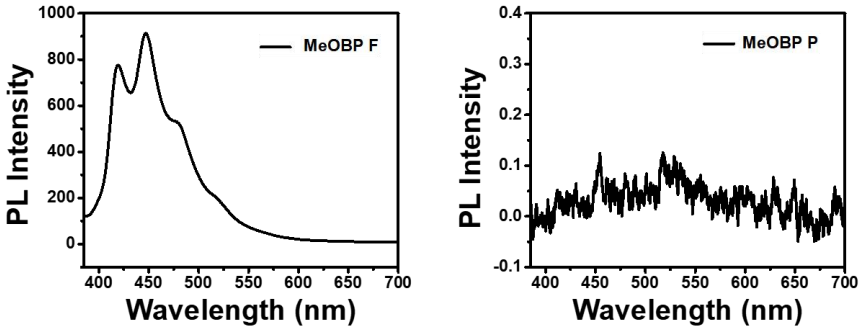

Figure S13. Steady-state emission (left) and delayed emission (right, 1 ms delay) spectra of the purified MeOBP matrices. The MeOBP matrices were purified by two cycles of recrystallization.

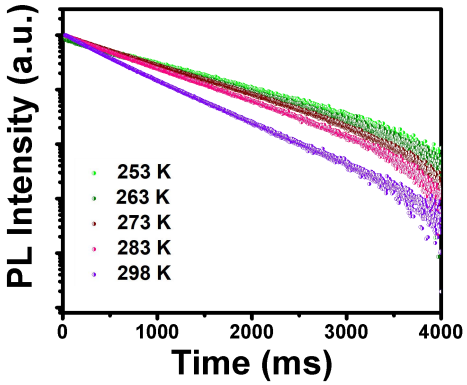

Figure S14. Temperature-dependent delayed emission decay of the $CorBF_2$-MeOBP-0.01% materials (monitored at 504 nm).

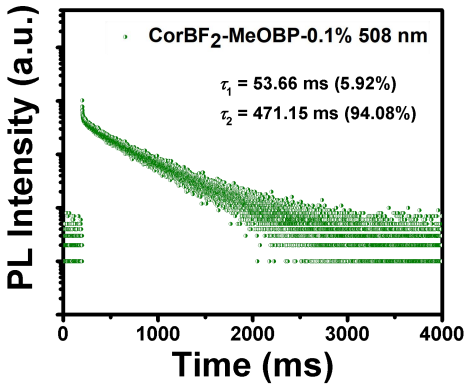

Figure S15. Room-temperature emission decay of $CorBF_2$-MeOBP-0.1% materials monitored at 508 nm.

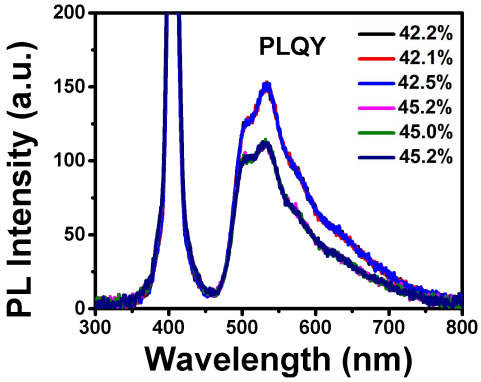

Figure S16. Photoluminescence quantum yield of $CorBF_2$-MeOBP-0.1% materials excited at 405 nm.

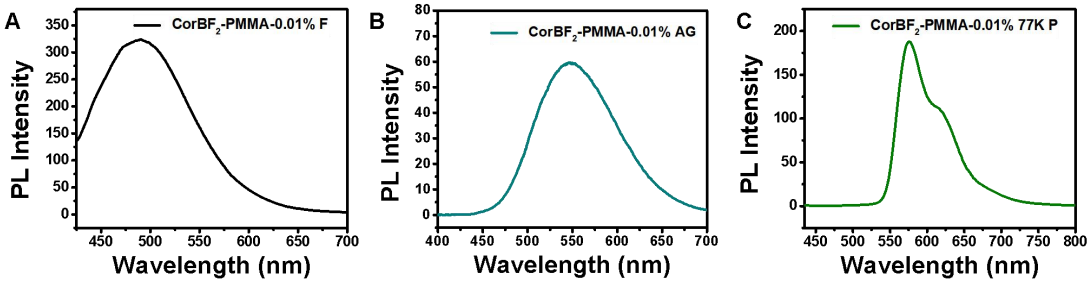

Figure S17. (A, B) Room-temperature steady-state and delayed emission spectra of the $CorBF_2$-PMMA-0.01% materials. (C) Delayed emission spectra of $CorBF_2$-PMMA-0.01% materials at 77 K.

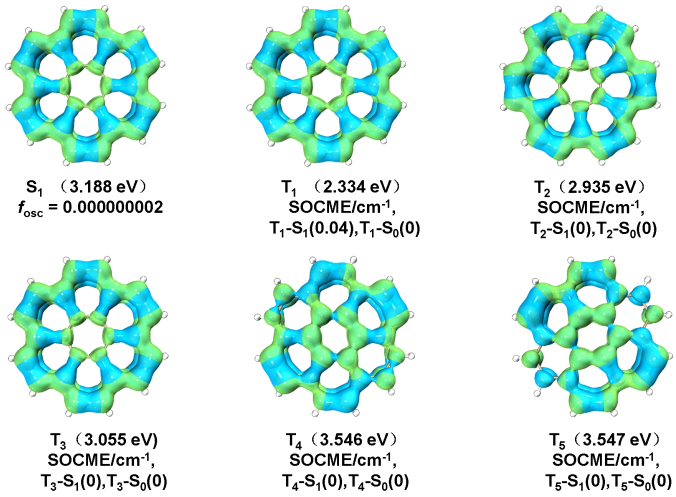

Figure S18. TD-DFT-calculated electron density difference of singlet and triplet excited states of coronene.

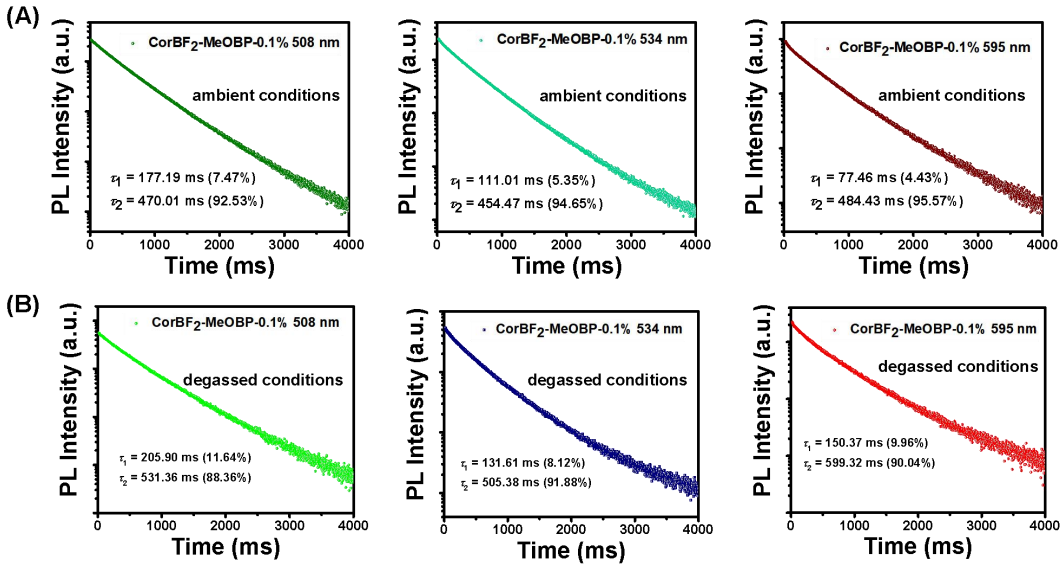

Figure S19. Room-temperature emission decay of $CorBF_2$-MeOBP-0.1% melt-cast samples under ambient conditions (A) and in degassed conditions (B) monitored at 508 nm, 534 nm and 595 nm.

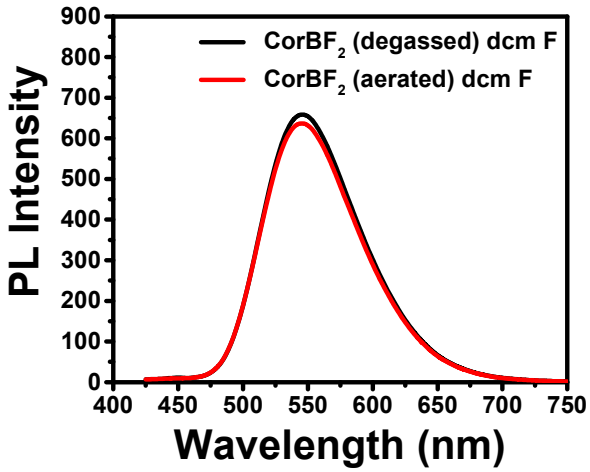

Figure S20. (A) Room-temperature steady-state emission spectra of $CorBF_2$ in dichloromethane solution (black line, in degassed condition; red line, in aerated condition).

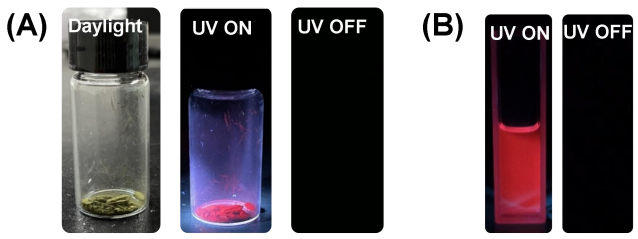

Figure S21. (A-B) Photographs of R_1 powders (A) and R_1 in dichloromethane (B) at room temperature under 365 nm UV light and after removal of the UV light.

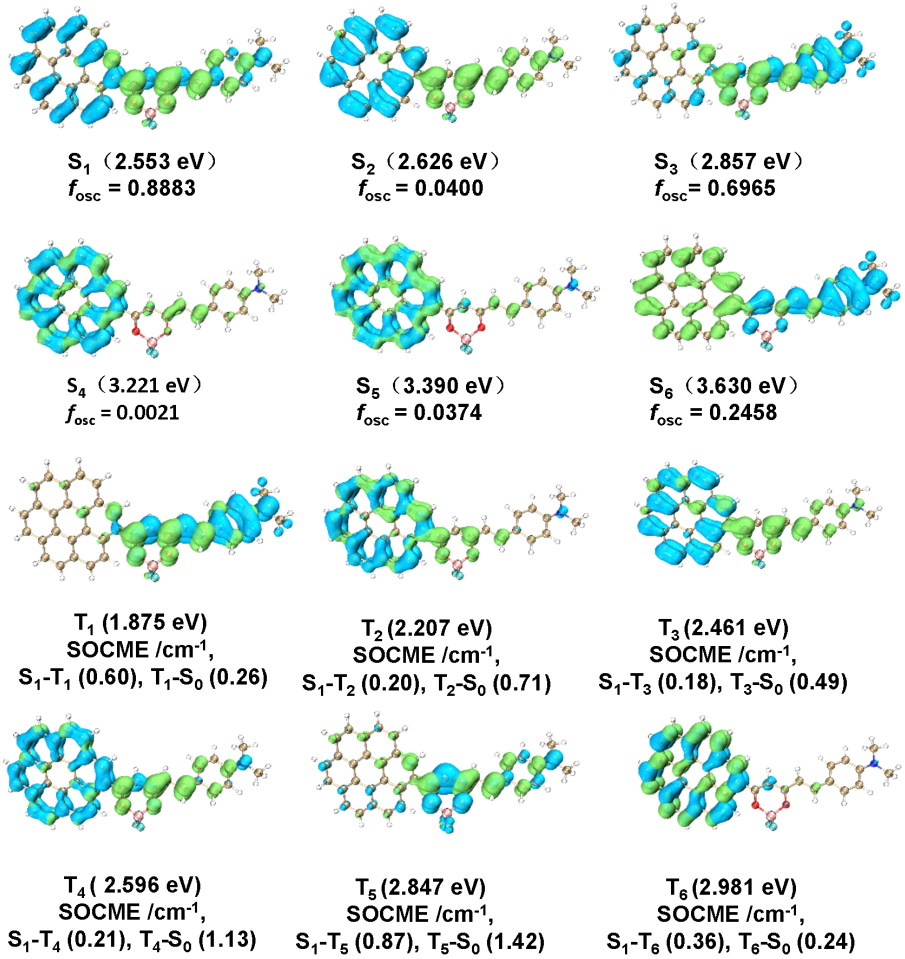

Figure S22. TD-DFT-calculated electron density difference of singlet and triplet excited states of R_1.

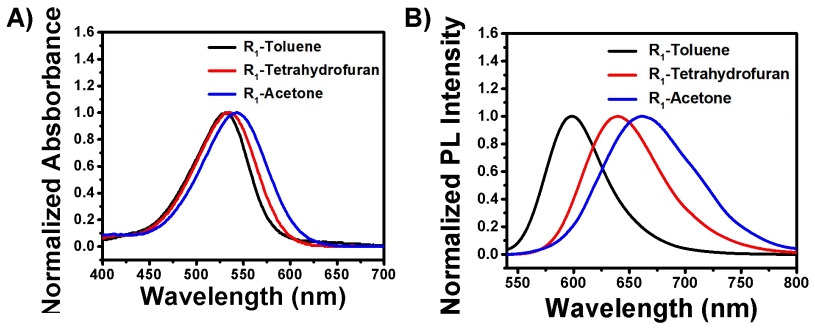

Figure S23. (A) UV-vis spectra of R_1 in toluene, tetrahydrofuran and acetone solutions. (B) Steady-state emission spectra of R_1 in toluene, tetrahydrofuran and acetone solutions.

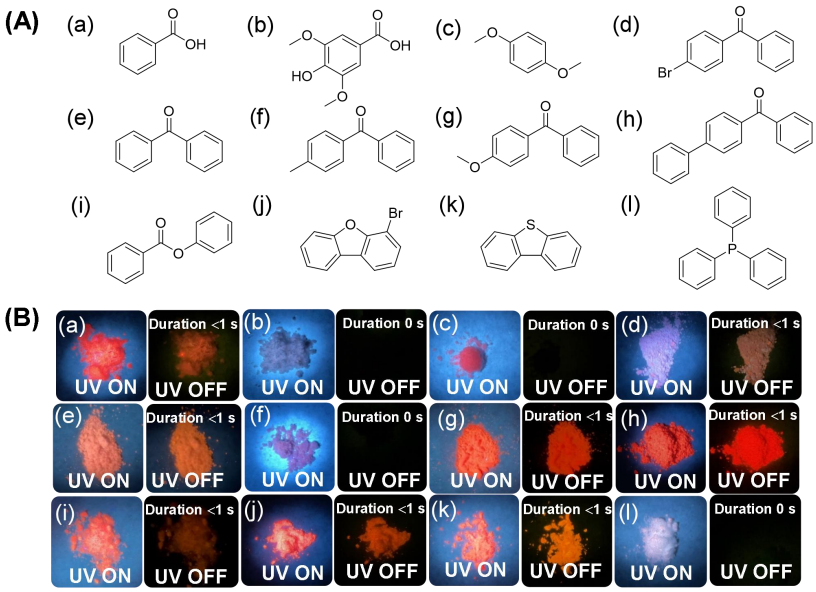

Figure S24. (A-B) The chemical structural formula (A) of organic matrices and photographs (B) of R_1-matrix-0.002% powders under 365 nm UV light and after removal of the UV light. Duration refers to the lasting time of afterglow after removal of the UV light.

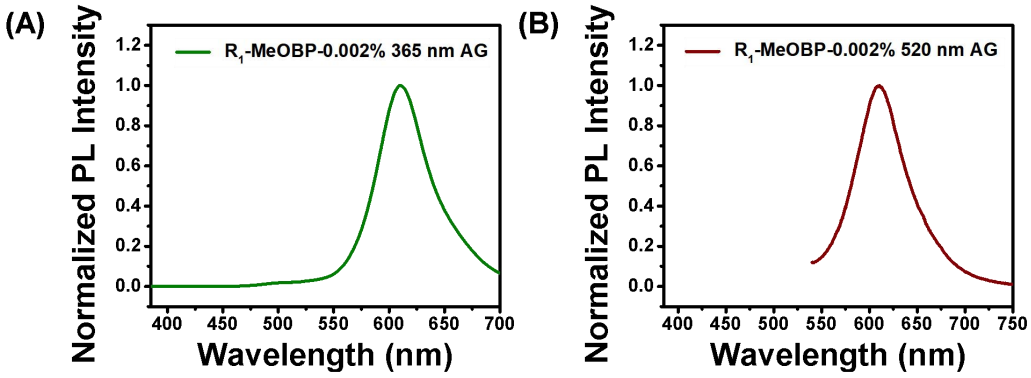

Figure S25. (A-B) Room-temperature delayed emission spectra of R_1-MeOBP-0.002% powders excited by 365 nm UV excitation source (A) and 520 nm UV excitation source (B).

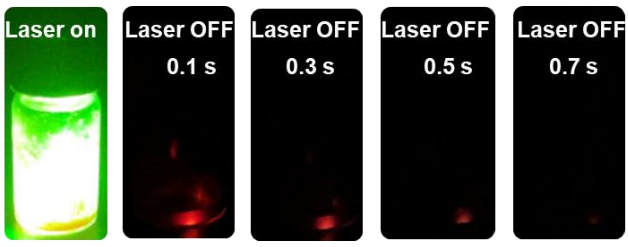

Figure S26. Photographs of R_1-MeOBP-0.02% powders at room temperature under 532 nm laser and after ceasing the 532 nm laser.

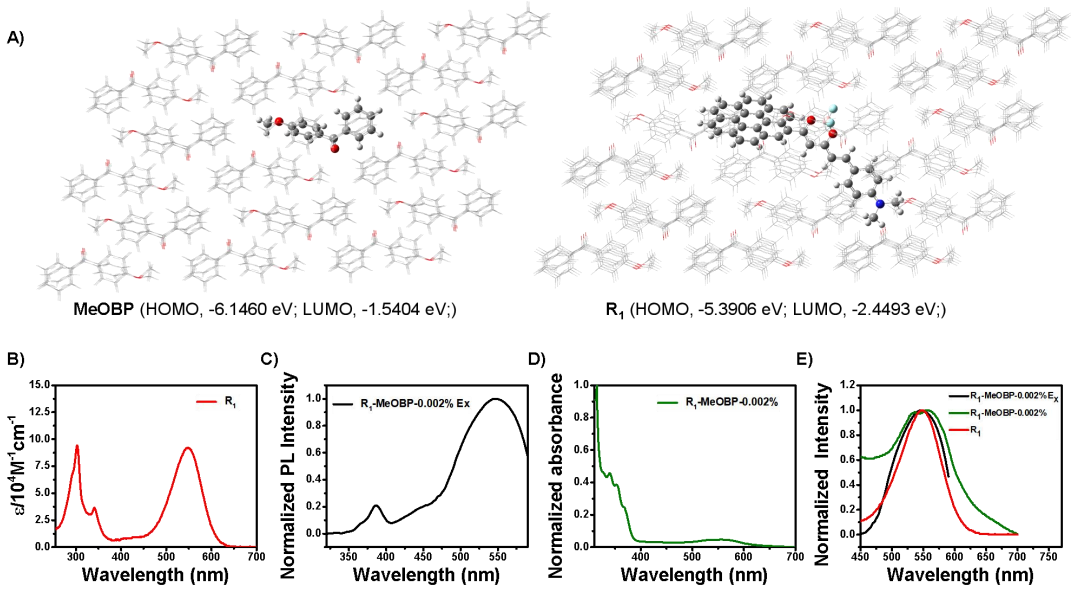

Figure S27. (A) Theoretical calculations to estimate the HOMO and LUMO levels of R_1 in MeOBP matrix. To investigate the electronic properties of R_1 and MeOBP embedded in the MeOBP matrix, the QM/MM model (MM method with the UFF force field) was built from the single-crystal structure of MeOBP. The HOMO and LUMO levels of R_1 and MeOBP in MeOBP matrix have been estimated from TD-DFT calculation on Gaussian 16 program with B3LYP functional and 6-31G(d,p) basis set. (B-D) UV-vis spectra of R_1 in dichloromethane solutions (B), excitation spectra in the range of 320 nm to 590 nm monitored at 610 nm (C) of R_1-MeOBP-0.002% samples and UV-vis spectra of R_1-MeOBP-0.002% melt-cast films (D). (E) The normalized spectra of (B) to (D).

Figure S28. Photographs of R_1-MeOBP-0.01% powders at 77 K under 532 nm laser and after removal of the laser.

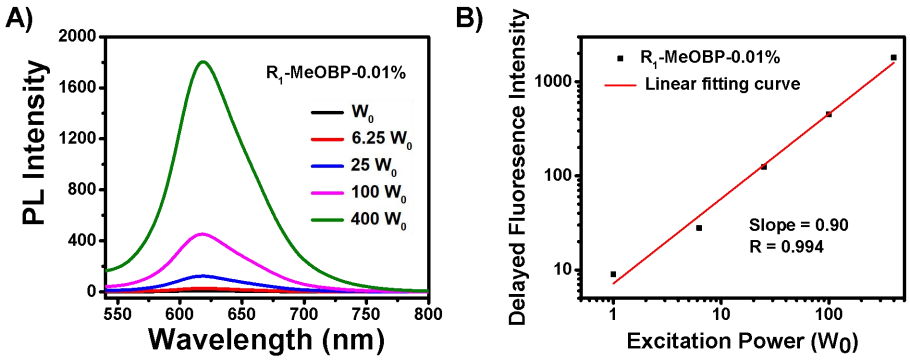

Figure S29. (A-B) Power-dependent delayed fluorescence spectra of R_1-MeOBP-0.01% samples (A). It is found that the intensity of delayed fluorescence of the afterglow materials exhibit a quasi-linear dependence on the excitation dose, which further support the TADF mechanism (B).

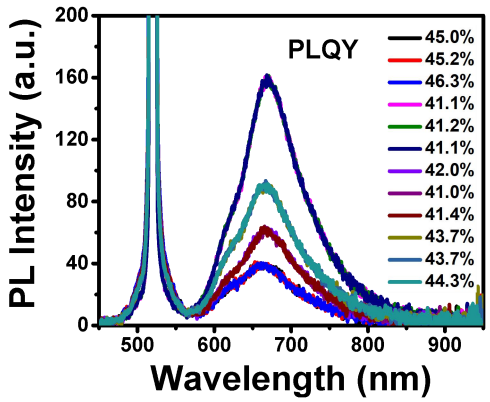

Figure S30. Photoluminescence quantum yield of R_1-MeOBP-0.01% materials excited at 520 nm.

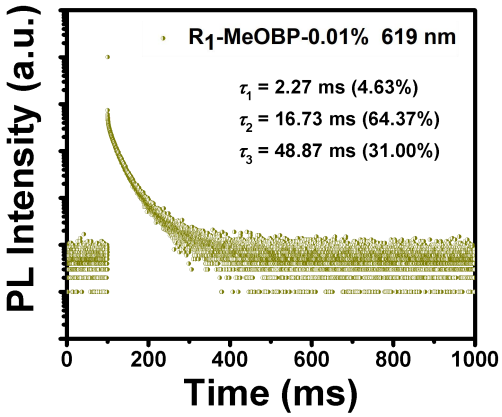

Figure S31. Room-temperature emission decay of R_1-MeOBP-0.01% materials monitored at 619 nm. The excited decay profiles were recorded by using time-correlated single photon counting technique (TCSPC) on a Edinburgh FLS1000 fluorescence spectrometer.

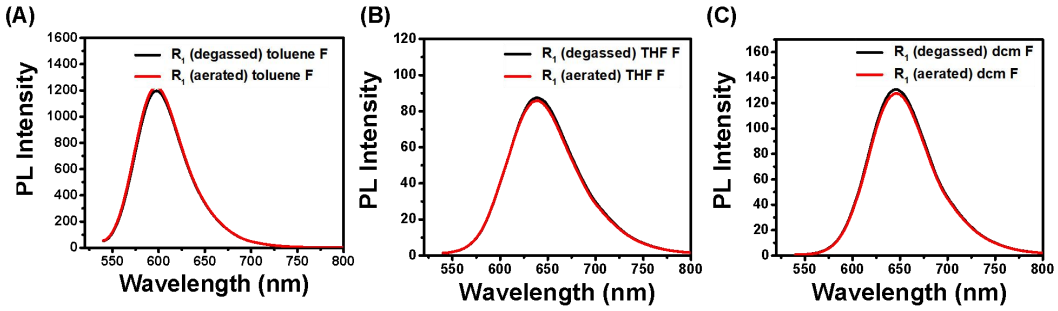

Figure S32. (A-B) Room-temperature steady-state emission spectra of R_1 solution in toluene (A), THF (B) and DCM (C) (black line, in degassed condition; red line, in aerated condition).

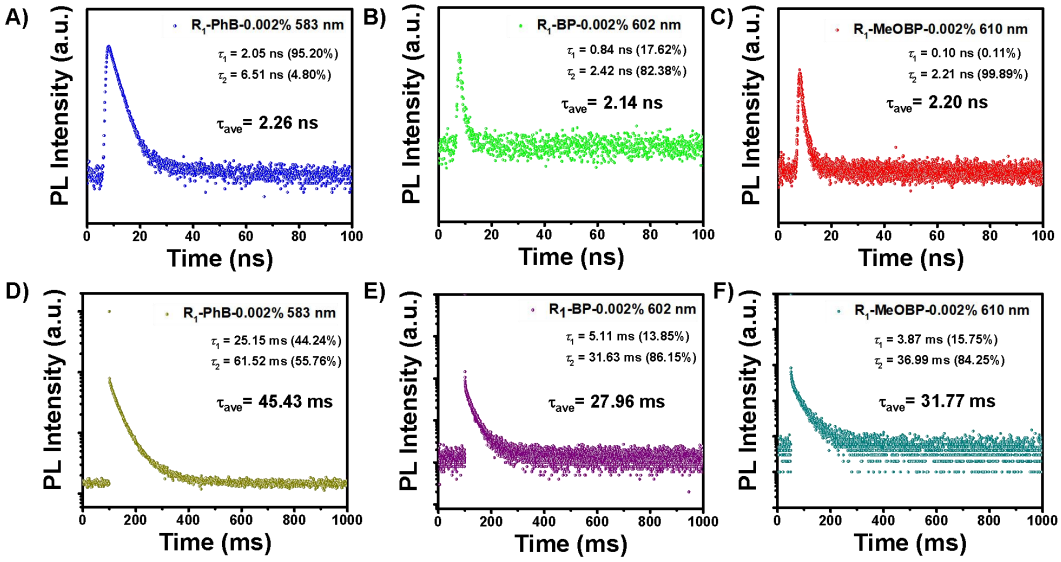

Figure S33. (A-C) Room-temperature prompt fluorescence decay of R_1-matrix-0.002% samples monitored at their emission maxima: (A) PhB, measured at 583 nm; (B) BP, measured at 602 nm; (C) MeOBP, measured at 610 nm. (D-F) Room-temperature emission decay of R_1-PhB-0.002% materials monitored at 583 nm (PhB, D), R_1-BP-0.002% materials monitored at 602 nm (BP, E) and R_1-MeOBP-0.002% materials monitored at 610 nm (MeOBP, F). These excited state decay profiles were recorded by using time-correlated single photon counting technique (TCSPC) on a Edinburgh FLS1000 fluorescence spectrometer equipped with a picosecond pulsed diode laser and microsecond flash Xe lamp.

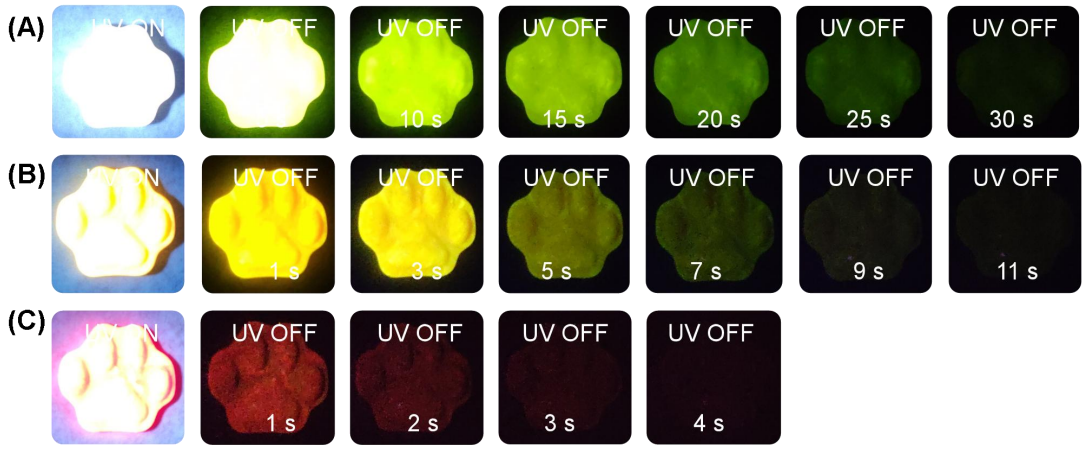

Figure S34. (A-C) Photographs of Cor-MeOBP-0.1% (A), CorBF$_2$-MeOBP-0.1% (B), R$_1$-MeOBP-0.01% (C) afterglow objects under 365 nm UV light and after removal of UV excitation, respectively.

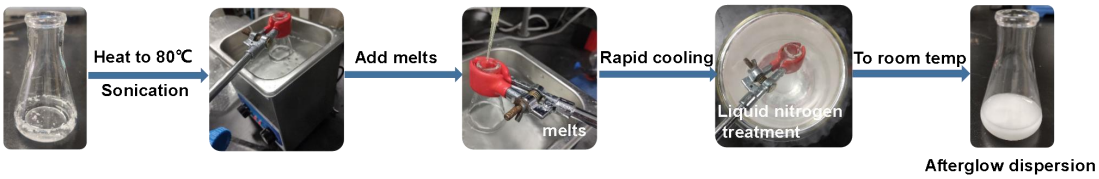

Figure S35. Procedures to prepare afterglow dispersion.

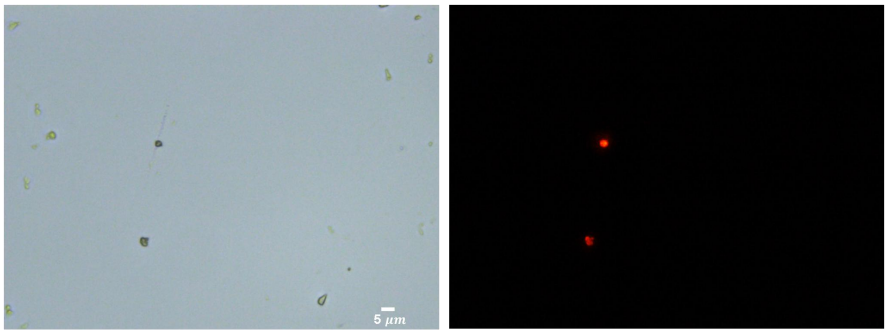

Figure S36. Images of the sphere-like micro-objects in the afterglow dispersion of R$_1$-MeOBP-0.02% captured by fluorescence microscope. The left images are recorded at bright field mode, while the right image collected at fluorescence mode (565 nm excitation source).

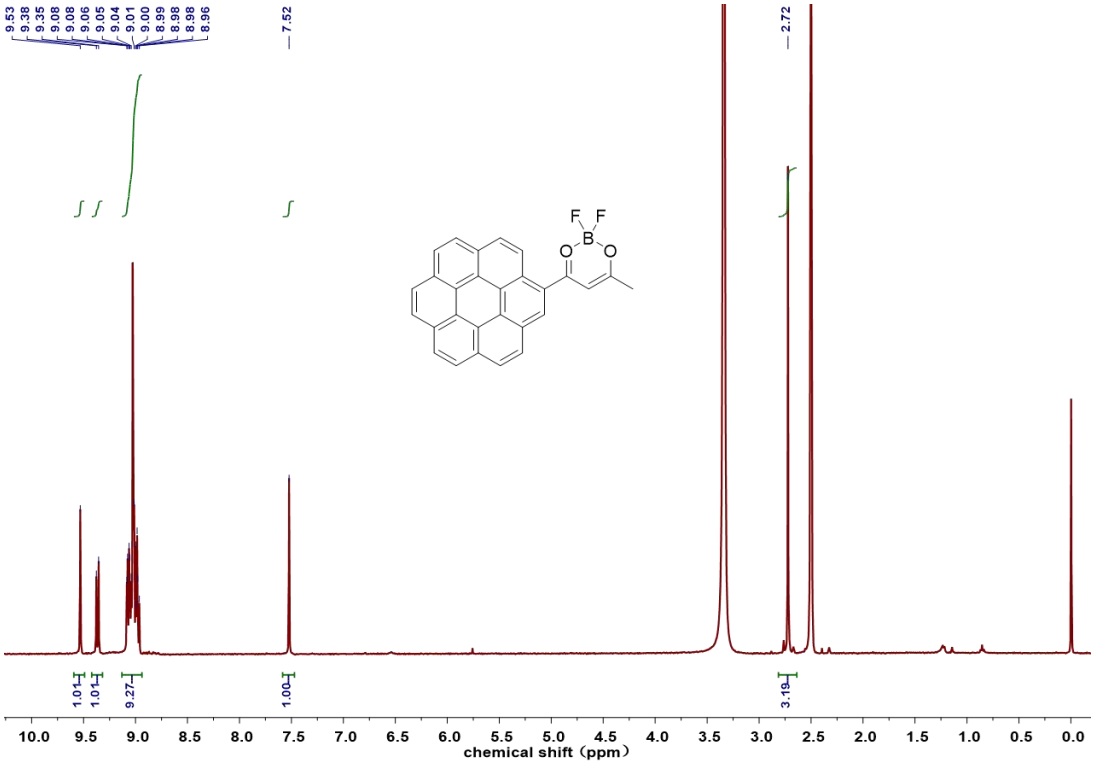

Figure S37. ^{1}H NMR spectrum of $CorBF_2$.

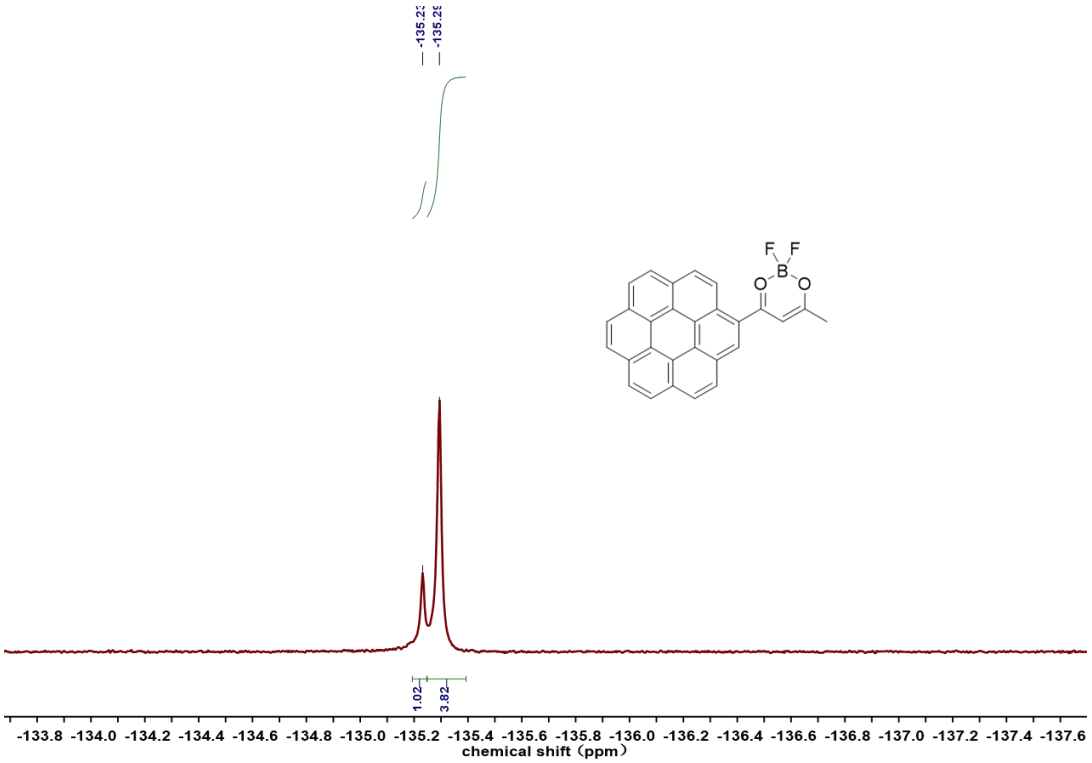

Figure S38. $^{19}F\{H\}$ NMR spectrum of $CorBF_2$.

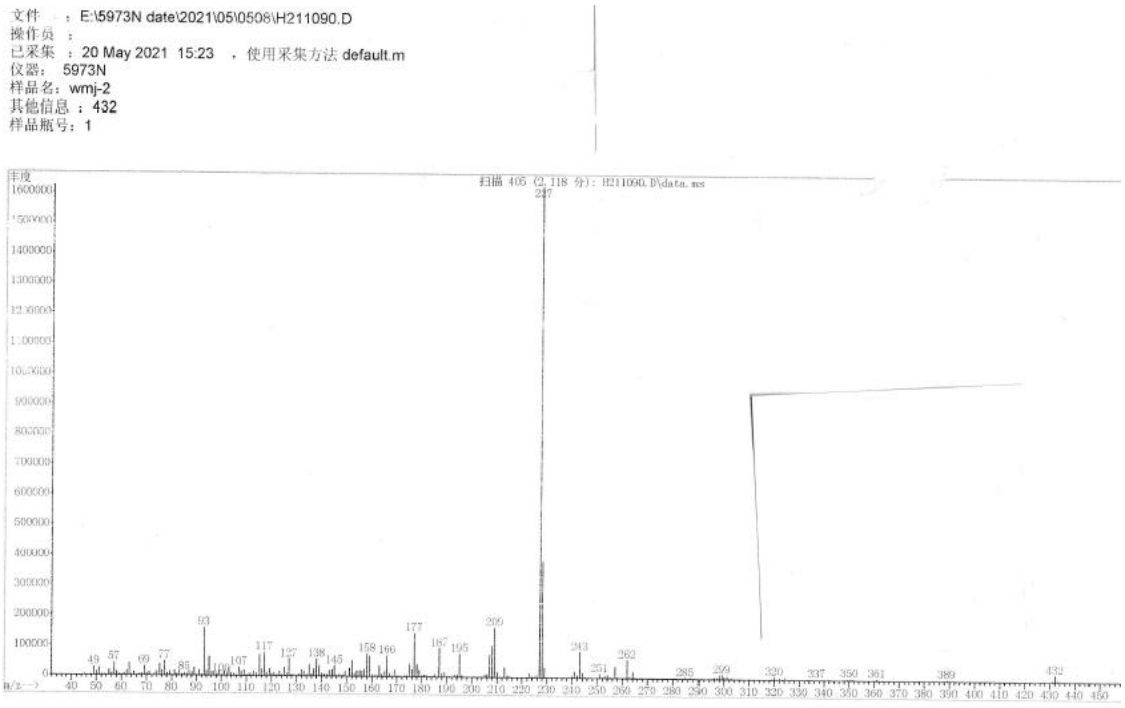

Figure S39. LRMS spectrum of $CorBF_2$.

National Center for Organic Mass Spectrometry in Shanghai
Shanghai Institute of Organic Chemistry
Chinese Academic of Sciences
High Resolution ESI-MS REPORT

Instrument: Thermo Scientific Q Exactive HF Orbitrap-FTMS

Card Serial Number: E221753

Sample Serial Number: wmj-yl

Operator: WHY Date: 2022/09/09

Operation Mode: Negative Ion Mode

Elemental composition search on mass 430.1096

m/z= 425.1096-435.1096

m/z	Theo. Mass	Delta (ppm)	RDB equiv.	Composition
430.1096	430.1097	-0.12	21.5	$C_{28}H_{14}O_2{}^{10}BF_2$

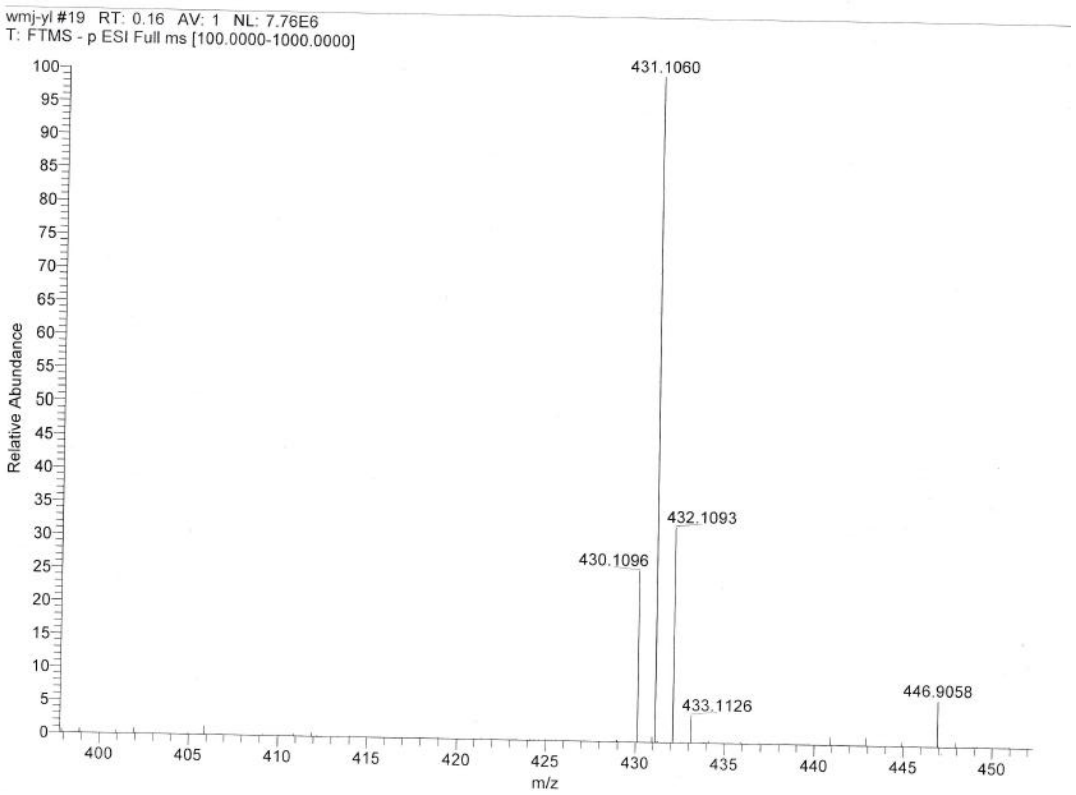

Figure S40. HRMS spectrum of $CorBF_2$.

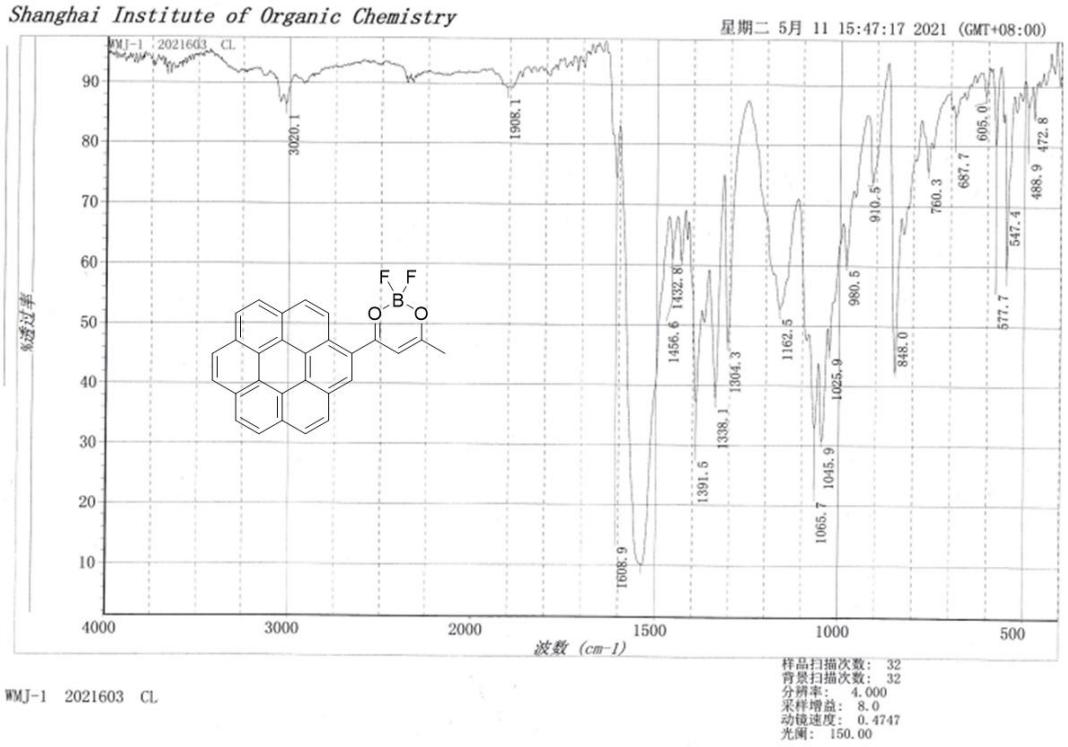

Figure S41. FT-IR spectrum of $CorBF_2$.

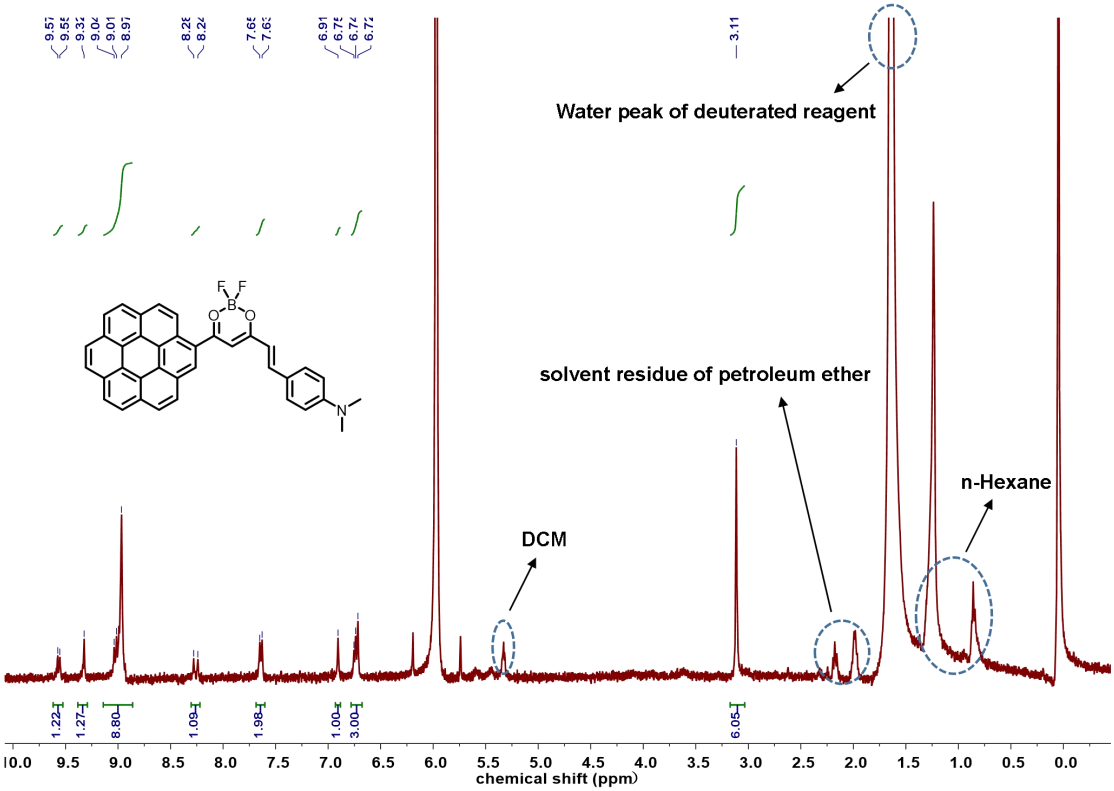

Figure S42. ^{1}H NMR spectrum of R_1.

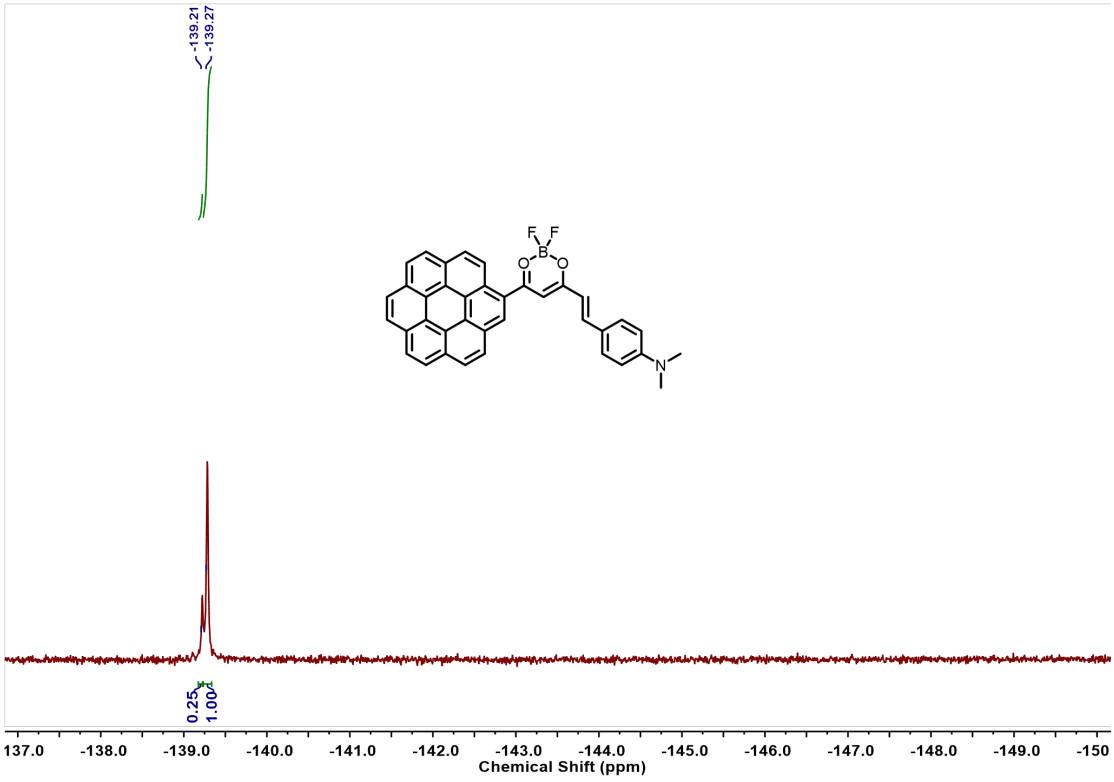

Figure S43. $^{19}F\{H\}$ NMR spectrum of R_1.

文件　：E:\5973N DATE\2021\07\0706\Snapshot\H211411.D
操作员　：
已采集　：7 Jul 2021　14:50　，使用采集方法 default.m
仪器：　5973N
样品名：WMJ-R1
其他信息　：563
样品瓶号：1

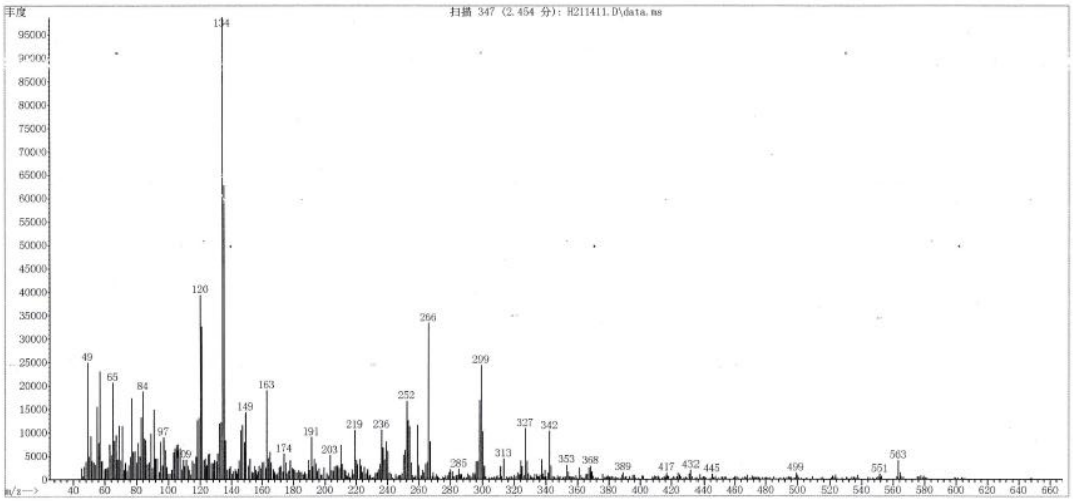

Figure S44. LRMS spectrum of R_1.

National Center for Organic Mass Spectrometry in Shanghai
Shanghai Institute of Organic Chemistry
Chinese Academic of Sciences
High Resolution ESI-MS REPORT

Instrument: Thermo Scientific Q Exactive HF Orbitrap-FTMS

Card Serial Number: E211712

Sample Serial Number: WMJ-R1

Operator: Songw Date: 2021/07/08

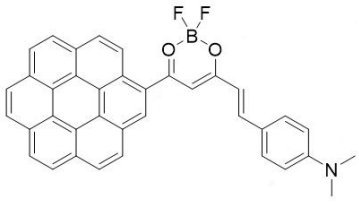

Operation Mode: ESI Positive Ion Mode

Elemental composition search on mass 585.1793

m/z= 580.1793-590.1793

m/z	Theo. Mass	Delta (ppm)	RDB equiv.	Composition
585.1793	585.1797	-0.70	25.5	$C_{37}H_{24}O_2N^{10}BF_2Na$
	585.1785	1.34	25.5	$C_{37}H_{26}O_4N_2Na$

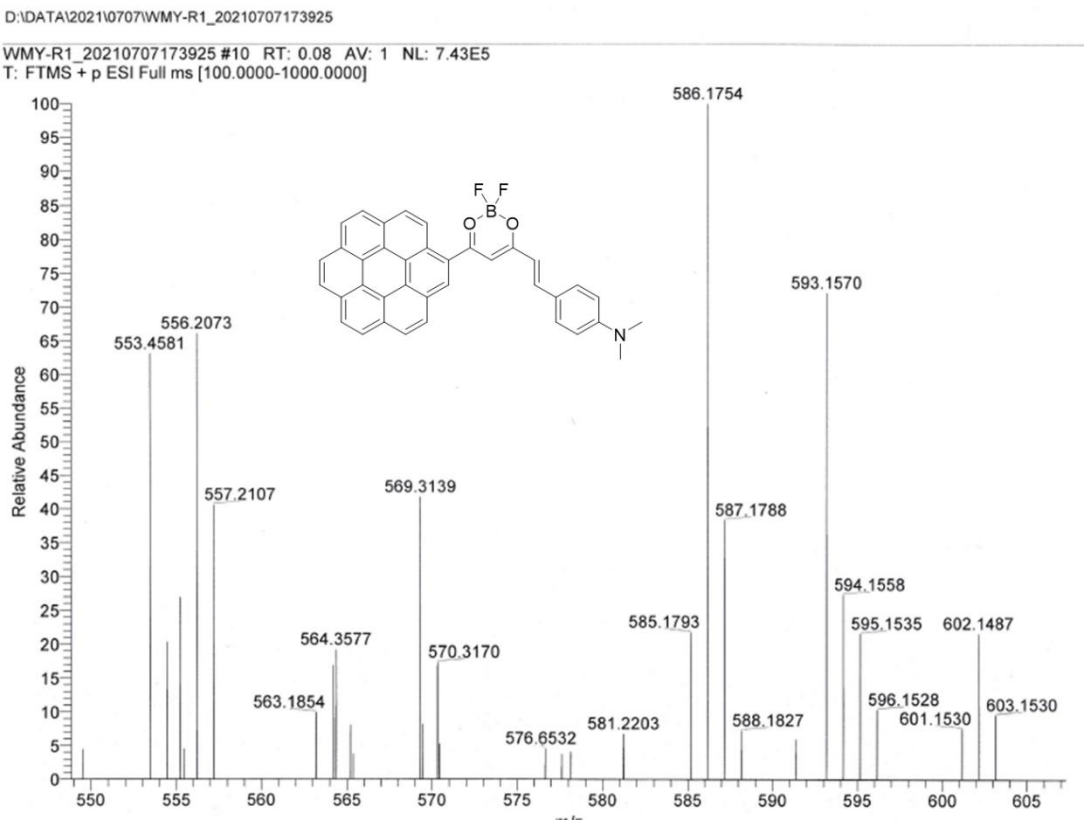

Figure S45. HRMS spectrum of R_1.

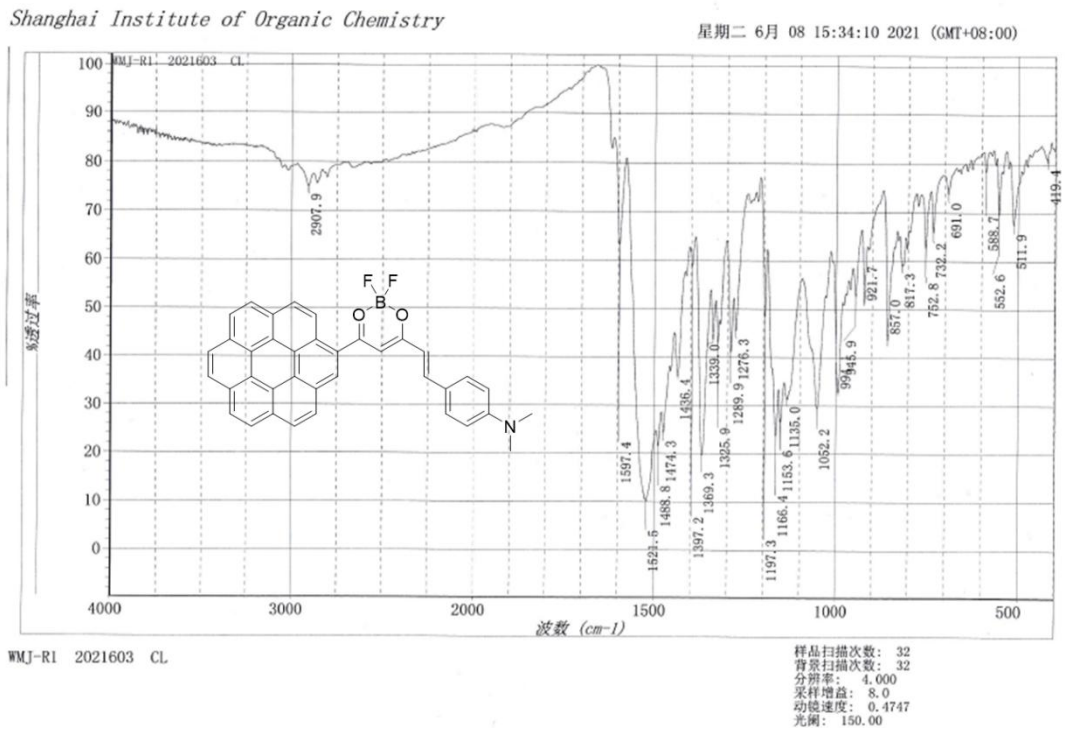

Figure S46. FT-IR spectrum of R_1.